


Flow-induced 2D nanomaterials intercalated aligned bacterial cellulose

Received: 28 September 2024

Accepted: 19 May 2025

Published online: 01 July 2025



M.A.S.R. Saadi¹, Yufei Cui², Shyam P. Bhakta ³, Sakib Hassan⁴,
Vijay Harikrishnan¹, Ivan R. Siqueira ⁵, Matteo Pasquali ^{1,5,6},
Matthew Bennett ³, Pulickel M. Ajayan ¹ & Muhammad M. Rahman^{1,7} ✉

Bacterial cellulose is a promising biodegradable alternative to synthetic polymers due to the robust mechanical properties of its nano-fibrillar building blocks. However, its full potential of mechanical properties remains unrealized, primarily due to the challenge of aligning nanofibrils at the macroscale. Additionally, the limited diffusion of other nano-fillers within the three-dimensional nanofibrillar network impedes the development of multifunctional bacterial cellulose-based nanosheets. Here, we report a simple, single-step, and scalable bottom-up strategy to biosynthesize robust bacterial cellulose sheets with aligned nanofibrils and bacterial cellulose-based multifunctional hybrid nanosheets using shear forces from fluid flow in a rotational culture device. The resulting bacterial cellulose sheets display high tensile strength (up to ~436 MPa), flexibility, foldability, optical transparency, and long-term mechanical stability. By incorporating boron nitride nanosheets into the liquid nutrient media, we fabricate bacterial cellulose-boron nitride hybrid nanosheets with even better mechanical properties (tensile strength up to ~553 MPa) and thermal properties (three times faster rate of heat dissipation compared to control samples). This biofabrication approach yielding aligned, strong, and multifunctional bacterial cellulose sheets would pave the way towards applications in structural materials, thermal management, packaging, textiles, green electronics, and energy storage.

Growing concern over the harmful effects of petroleum-based, non-degradable materials on the environment has intensified the demand for sustainable alternatives, such as natural or biomaterials^{1–5}. Cellulose, a polysaccharide with glucose-based repeating unit, has emerged as a potential biomaterial that is naturally abundant, biodegradable, and biocompatible^{2,4}. Specifically, bacterial cellulose (BC), produced from aerobic bacteria, including *Acetobacter* and *Agrobacterium*, can be engineered to exhibit desirable and controllable mechanical properties by leveraging its nanoscale structure. These bacteria produce β -1,4-glucan chains and form cellulose

microfibrils^{6,7}, which are further arranged in a 3D reticulated network, providing BC sheets with high porosity, enhanced tensile strength, and high water retention capacity⁸. Unlike plant cellulose, BC is free from hemicellulose, lignin, and other biogenic components, is highly pure, and has higher crystallinity^{6,9}. These intrinsic characteristics of BC, along with its flexibility, optical transparency, and low thermal expansion coefficient, make it an attractive candidate for numerous applications such as biomedical, healthcare devices, packaging, bioelectronics, photonics, energy storage, and structural material, etc^{2,4,10–18}.

¹Department of Materials Science and NanoEngineering, Rice University, Houston, TX, USA. ²Department of Bioengineering, Rice University, Houston, TX, USA.

³Department of Biosciences, Rice University, Houston, TX, USA. ⁴Department of Electrical and Computer Engineering, Rice University, Houston, TX, USA.

⁵Department of Chemical and Biomolecular Engineering, Rice University, Houston, TX, USA. ⁶Department of Chemistry, Rice University, Houston, TX, USA.

⁷Department of Mechanical and Aerospace Engineering, University of Houston, Houston, TX, USA. ✉ e-mail: maksud@uh.edu

Despite the recent demonstration of several emerging applications of BC, its full potential is yet to be realized owing to several factors. One of the major limitations of BC macrostructure as a sheet is its low mechanical properties, e.g., strength and stiffness, compared to their theoretical values^{1,15,19}. The building block of BC, i.e., ribbon-shaped individual nanofibrils, possesses extraordinary theoretical mechanical properties such as tensile strength of 6–7 GPa²⁰ and Young's modulus of 120–140 GPa²¹ due to the highly aligned molecular chain. However, translating these exceptional properties to macro-scale bulk material (BC sheet) is challenging. This stems mainly from the misalignment of the nanofibrils in the macroscopic or bulk counterparts, coupled with boundaries, voids, defects, and entanglements among nanofibrils^{1,15,21}. Conventional cultivation of BC yields a randomly oriented web-like fibril network due to the free movement of the bacteria, which contributes to the challenges of translating mechanical properties from the nano to macro scale. Several research efforts have been devoted to improving the alignment of BC nanofibrils and, hence, anisotropic mechanical properties of BC sheets, including template molding, electromagnetic field-assisted cultivation, post-harvest processing, etc.^{1,15,22–26}. Among these, post-harvest processing—particularly stretching the BC hydrogel—has garnered significant attention. For instance, Rahman et al.¹ increased the BC nanofibrils alignment using a 3D printed polydimethylsiloxane (PDMS) mold that confined the movement of the bacteria inside the groove of the mold and, hence, improved the orientation of fibers during sheet formation¹. The resulting BC sheet was then wet-stretched up to 20% to increase the degree of anisotropy, and consequently, the mechanical strength of the BC sheets improved to 260 MPa. Similarly, Wang et al.¹⁵ reported the production of an ultra-strong cellulose film after a staggering 40% of wet drawing strain with the aid of vigorous shaking. Thus, post-harvest stretching has demonstrated significant potential for meeting application demands by enabling targeted mechanical enhancements in BC sheets. However, post-harvest stretching requires additional equipment for controlled stretching. It might also induce local damage in the BC hydrogel structure due to their inherent kinks and entanglement during the exertion of force^{27,28}. Additionally, existing techniques for aligning BC nanofibrils are limited in their ability to simultaneously impart added functional properties (e.g., thermal, electrical, optical, etc.) to BC sheets—features that are essential for expanding their application potential. A mechanically robust and multifunctional BC sheet could unlock a broader range of applications compared to those currently available. Therefore, to address the demands of advanced applications, it remains imperative to explore strategies that can concurrently overcome mechanical limitations and integrate functional properties.

One approach to enhance both the mechanical and functional attributes of BC is through the incorporation of nanoscale building blocks with exceptional properties into the BC nanofibrillar network, thereby developing BC-based hybrid nanosheets^{29–31}. The conventional process of fabricating BC-based hybrid nanosheets involves the disintegration of 3D network structure for solution processing, which seriously impairs the mechanical performance of BC³². Static fermentation, on the other hand, failed to produce a uniform hybrid system due to (1) the diffusion-limited transfer/intercalation of nanoscale units from the liquid medium to the upper surface layer of newly grown BC and (2) the dispersion stability of the secondary nano inclusions³³. Although aerosol/in situ spray-assisted synthesis of BC can infuse multifunctionality, the free motion of bacteria on the solid/liquid substrate cannot produce aligned and strong BC in a single step^{33,34}. Consequently, BC structures with concurrent structural and functional attributes could not be realized due to the lack of distributed secondary nanoscale building blocks in the BC network and the misalignment of the nanofibrils. Therefore, additional work is required to develop an assembly strategy for generating BC-based robust multifunctional nanosheets.

Herein, we report a facile, sustainable, and single-step bottom-up biosynthesis technique based on fluid flow-assisted shear alignment, which enables in situ layer-by-layer deposition of anisotropic BC nanofibrils and BC-based hybrid nanosheets. Specifically, we introduce a custom-designed rotation culture device where cellulose-producing bacteria are cultured in a cylindrical oxygen-permeable incubator continuously spun using a central shaft to produce directional fluid flow. This flow results in consistent directional travel of the bacteria that significantly improves nanofibril alignment in bulk BC sheets. The BC sheets from the rotation culture device displayed high tensile strength with excellent flexibility, foldability, optical transparency, and long-term mechanical stability. The improvement in the nanofibrillar alignment and its effect on the mechanical properties of the BC sheets were investigated using a holistic approach of multiscale experiments and theory. We also overcome the limitations of BC-based hybrid nanosheet fabrication by the simultaneous directional growth of BC nanofibrils and distribution of nanoscale building blocks, in this case, boron nitride (BN) nanosheets (BNNS), within the BC network. The rotational flow provides dispersion stability to the BNNS in the nutrient media that homogeneously distribute them within the 1D BC nanofibrillar network, forming a robust 1D–2D BCBN hybrid nanosheet with excellent mechanical and thermal properties. Our approach to producing BC and BC-based hybrid nanosheets could open pathways towards its ubiquitous utilization in myriad applications ranging from structural, thermal, packaging, textile, green electronics, and energy storage.

Results and discussion

Biosynthesis of bacterial cellulose sheet in rotational culture device

The liquid medium containing the bacterial strain, *Novacitomonas hansenii* ATCC 53582³⁵, and the culture nutrients were placed in a custom-designed rotational culture device (Fig. 1a, and Supplementary Fig. 1), which consist of five main parts: base, cap, shaft, tube and a motor (Supplementary Fig. 2 and Supplementary Movie 1 and 2). The device schematic and dimensions are depicted in Supplementary Fig. 3. The cylindrical body of the device was made using PDMS, which is oxygen-permeable to facilitate the growth of the aerobic bacterial strain. The PDMS tube was sealed tightly by a 3D-printed cap and base to prevent diffusion of oxygen (thus preventing the formation of BC on top and bottom of the liquid) and fluid leakage from the bottom of the system, respectively. The cap also enables the connection (through a hole) between the DC motor (glued to the top of the cap) and a 3D-printed rectangular shaft attached between the cap and the base (Supplementary Fig. 2). The shaft sits on a protrusion from the center of the base, which holds it at the center of the PDMS tube. The DC motor supplies power to rotate the shaft around the center axis, creating a continuous rotational fluid flow in the device. The shaft pushes the nutrient media with cellulose-producing bacteria to move along the same direction of fluid rotation, thus producing fluidic shear forces between the edge of the shaft and the inner walls of the PDMS tube. The inner walls of the PDMS tube, where oxygen availability is the highest inside the bioreactor, act as the substrate for the formation of BC nanofibrils (since this class of bacteria requires oxygen for their survival and, hence, move towards the highest oxygen gradient) (Fig. 1b). Thus, BC hydrogel pellicle with anisotropic nanofibrillar alignment is produced on the inner surface of the PDMS tube (Fig. 1c). Once the BC nanofibrils are synthesized and deposited, they form a hydrogen-bonded network that stabilizes the fibrils in their aligned configuration. In the wet state, the strong interfibrillar hydrogen bonding prevents the nanofibrils from relaxing back to a random orientation. The rotation speed for our experiment was optimized at 60 rpm based on the mechanical properties of the BC sheets obtained from different rotational speeds (Supplementary Fig. 4). After 10 days of culture at a constant 60 rpm rotation speed, we collected the



Fig. 1 | Fabrication of bacterial cellulose (BC) in rotation culture device.

a Schematic of the rotational culture device for producing aligned BC and the key stages in the rotational process. The red arrow shows the direction of BC alignment. **b** Longitudinal cross-sectional view (i), top view (ii) and zoomed-in cross-sectional view (iii) of the rotational culture device shown in (i) during the production of aligned BC. **c** Optical photographs of the rotational device during culture before

and after cellulose formation. **d** BC tubular pellicle (i) grown on polydimethylsiloxane (PDMS) tube surface after culture period and (ii) on a glass plate after washing. The red arrow shows the direction of BC alignment. **e** Highly transparent BC sheet after drying through which the logo and letter “RICE” can be easily seen. The red arrow shows the direction of BC alignment.

tubular BC hydrogel from the rotation culture device and immediately washed it with 0.5 M NaOH to remove residual bacteria, followed by DI water rinse (Fig. 1d). We dried the BC samples at room temperature by sandwiching them between two Whatman filter papers. This drying method resulted in no lateral shrinkage in the X and Y directions, while the samples exhibited ~98% shrinkage along the Z-axis. After drying, the BC sample was highly transparent (Fig. 1e) and flexible enough to be easily folded to make an origami plane (Supplementary Fig. 5). Also, after unfolding, the sample retained its structural integrity, showing no fracture, and the folding lines were almost invisible and recoverable. For our bioreactor configuration and a growth period of 10 days, the dry BC sheet yield was determined to be 7.5 ± 0.9 mg/day. Note that the yield in this case was not optimized and can be influenced by factors such as oxygen availability (exclusively through the PDMS tube), dynamic growth conditions, growth period, and the bioreactor design³⁶.

Alignment in bacterial cellulose sheet

Traditionally, BC is synthesized using a static culture which produces BC sheets with random fibrillar alignment due to random motion of the bacteria. With random alignment of the nanofibrils, BC sheets fail to utilize the full mechanical strength of the fibrils. Therefore, the rotational culture device was designed to produce BC sheets with anisotropic nanofibrillar alignment, which generally leads to excellent mechanical properties. To understand the degree of alignment of the BC nanofibrils from rotation culture, we performed wide-angle X-ray scattering (WAXS) and compared it to BC grown in static culture (Fig. 2a). We observed in both cases that a diffraction peak at $q = 1.25 \text{ \AA}^{-1}$ ($2\theta = 17.6^\circ$) was aligned along the equatorial direction and was well separated from other peaks (Fig. 2a–ii, v). Therefore, we fit this peak to determine the extent of the orientation of the cellulose (Fig. 2a–iii, vi). From the fit, we calculate Herman's Orientation (HO) parameters, whose value ranges from 0 to 1, indicating random and perfect orientation, respectively^{37–39}. From the calculation, we found that the HO parameter for the rotational BC is -0.489, and for static BC is 0.027. Therefore, this increased HO value confirms the excellent alignment of nanofibrils in the BC grown from rotation culture. To visualize and further confirm BC nanofibril alignment inside sheets formed in the rotation culture device, the morphology of the BC sheets (both static and rotational) was investigated under high-resolution scanning electron microscope (SEM). The BC nanofibrils produced in the rotation device exhibited alignment and compactness as compared to the randomly oriented BC fibrils in the static culture sheet (Fig. 2b). Such alignment and compactness stem from the shear flow in the gap between the rotating shaft and the inner wall of the tube. The atomic force microscope (AFM) images also clearly indicate that the nanofibrils in the BC network become highly oriented for the rotational device samples (Fig. 2b inset). Finally, polarized light is a well-known methodology to assess a material's anisotropy or alignment⁴⁰. Typically, birefringence (a dark-light pattern) can be obtained when an anisotropic or aligned sample is circularly rotated 45° . The minimum light intensity is obtained when the sample is placed at 0° from the incident polarized light, whereas the maximum light intensity appears when placed at 45° . As shown in Fig. 2c, static BC films did not exhibit light polarization at 0° and 45° (Fig. 2c–ii, v), confirming the random distribution of the fibrils. On the contrary, the rotational device-grown BC gave dark-light patterns of light when disposed at 0° and 45° from the incident polarized light beam, respectively (Fig. 2c–iii, vi), confirming the alignment of the BC nanofibrils.

Mechanical characterization and performance comparison of bacterial cellulose sheets

The mechanical performance of the BC sheets produced by the rotational device was evaluated by uniaxial tensile testing and compared with the BC sheets from static culture. Figure 3a compares the

representative tensile stress-strain curve for static and rotational BC sheets. Figure 3b and Table 1 show the statistical comparison of ultimate tensile stress (UTS), Young's modulus (YM), and toughness or work of failure (WoF)⁴¹ calculated from the stress-strain plots (Supplementary Fig. 6). Compared to static BC, the average tensile strength of the rotational BC sheets grew by ~137% (from 165.7 ± 5.9 MPa to 393.3 ± 30.5 MPa). We attribute this significant enhancement ($p = 0.00713$) in the tensile strength of the rotational BC sheets to the enhanced alignment of nanofibrils. Cellulose nanofibrils can carry more load when the loading direction is the same as the longitudinal direction of the fibrils (i.e., aligned fibrils between the tensile grips). The tilted or off-axis fibers undergo shear forces under tensile loading, leading to early fracture (Supplementary Fig. 7). Therefore, the control samples with randomly aligned BC fibrils experience more shear forces, resulting in decreased tensile properties. The alignment of the nanofibrils also aided in improving the elastic response of the BC sheets. From Fig. 3b, the average Young's modulus of rotational BC increased by ~96% (from 16.6 ± 1.5 GPa to 32.6 ± 2.3 GPa) than static BC ($p = 0.00118$). Note that a compliance correction procedure was performed to account for the effects of external compliance (e.g., machine compliance). Details of the compliance correction procedure can be found in Supplementary Information and Supplementary Fig. 8. The stress-strain plots of the static BC can be further analyzed to observe an interesting trend: a linear relationship with a steep slope (YM1) up to ~0.6% strain, followed by a slight curvature (decreasing stress) and then another linear relationship with a relatively low (compared to the first linear region) slope (YM2) at higher strain values up to the UTS (Fig. 3c). This suggests structural damage to the 3D network of static BC. Randomly oriented nanofibrils are expected to have more kinks and entanglements compared to aligned fibrils, which, when deformed, would result in structural damage in the form of bond breaking, early fiber (kink or entanglement) breakage, fiber sliding, twisting and breaking etc.^{27,28}. The onset of such fiber failure events is marked by a dotted circle in Fig. 3c. Consequently, for the static BC, YM2 (6.9 ± 0.7 GPa) is lower than YM1 (17.0 ± 3.3 GPa) by ~60%, suggesting a substantial decrease in the load-bearing capacity of the static BC beyond a limited % strain (~0.6% strain). On the contrary, when an aligned sample is strained, there is less local damage due to fewer kinks and entanglement compared to randomly aligned control samples during the exertion of force upon the chains. As a result, there is less structural damage and/or fiber failure in the rotational BC sheets compared to static BC. Thus, for the rotational BC, the reduction of YM2 (17.0 ± 3.3 GPa) from YM1 (32.6 ± 2.3 GPa) is relatively low (~48%). Note that YM2 of the rotational BC (17.0 ± 3.3 GPa) is significantly ($p = 0.0286$) higher (~146%) than YM2 of static BC (6.9 ± 0.7 GPa). This suggests that the rotational BC can carry significantly more load even at higher strain values due to less fiber failure. On the other hand, fewer fibers carry the tensile load at higher strain values for the static BC, resulting in a lower YM2 and, ultimately, UTS. Similarly, The toughness of the rotational BC quantified as the area under the stress-strain curve (also referred to as the WoF)⁴¹ exhibited a significant increase (~166%), rising from 178.5 ± 21.5 MJ/m³ for static BC to 475.2 ± 17.2 MJ/m³ for rotational BC ($p = 0.000148$). Additionally, the fracture strain of the BC produced using the rotational culture device was higher ($2.1 \pm 0.1\%$) compared to the BC obtained from static culture ($1.8 \pm 0.2\%$). This simultaneous enhancement of both strength and toughness is noteworthy, as these properties are typically considered mutually exclusive in materials engineering⁴². We hypothesize that the straightened nanofibrils in the rotational BC form a denser, less porous structure (Supplementary Fig. 9) with enhanced interaction among fibers via hydrogen bonding⁴³. Under tensile stress, these fibrils begin to slide relative to each other, with subsequent fiber pull-off and fracture leading to material failure. The fiber sliding/slippage for rotational BC under tensile loading becomes more energetic, compared to static BC, due to the enhanced interfibrillar interaction facilitated by more

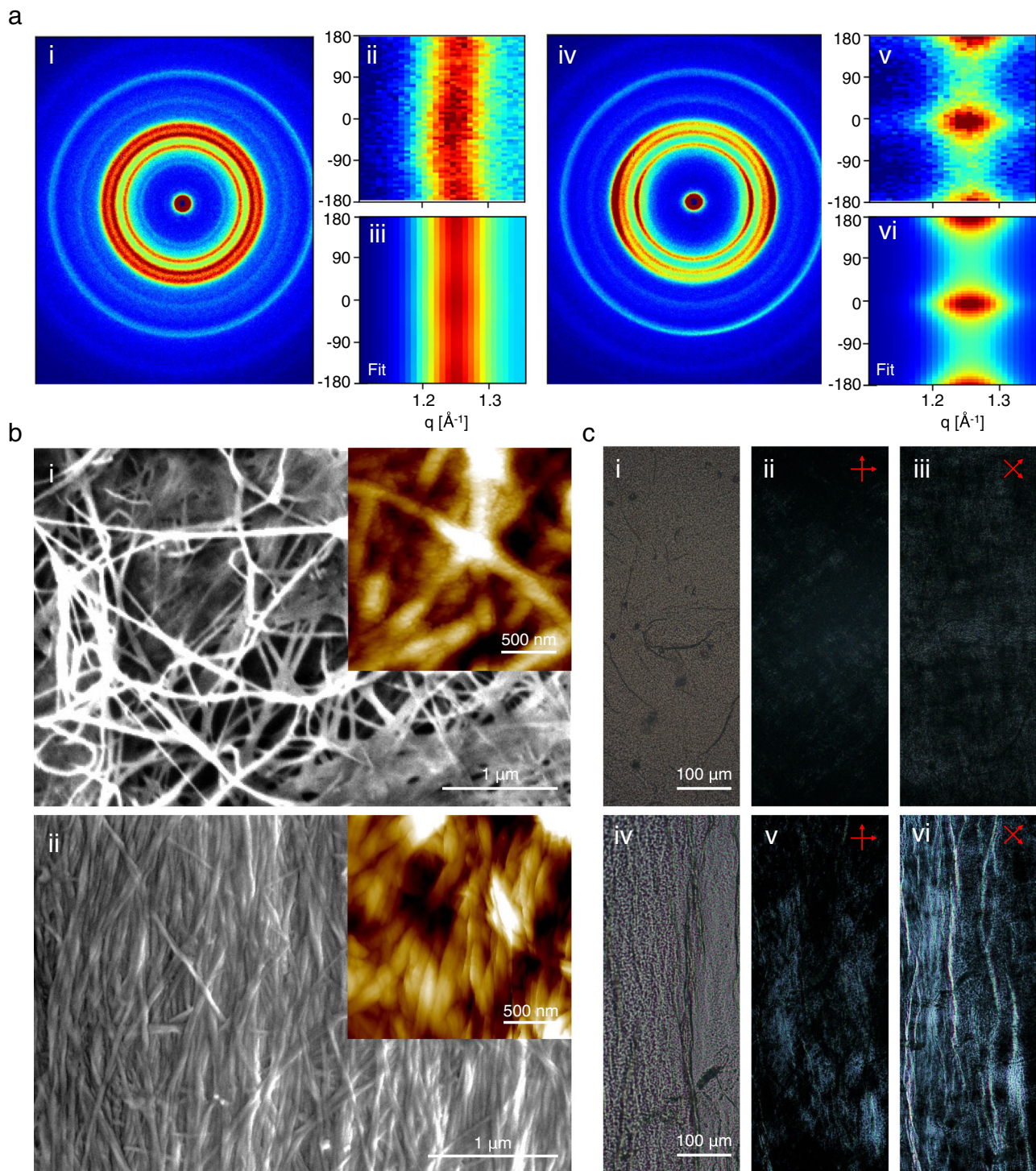
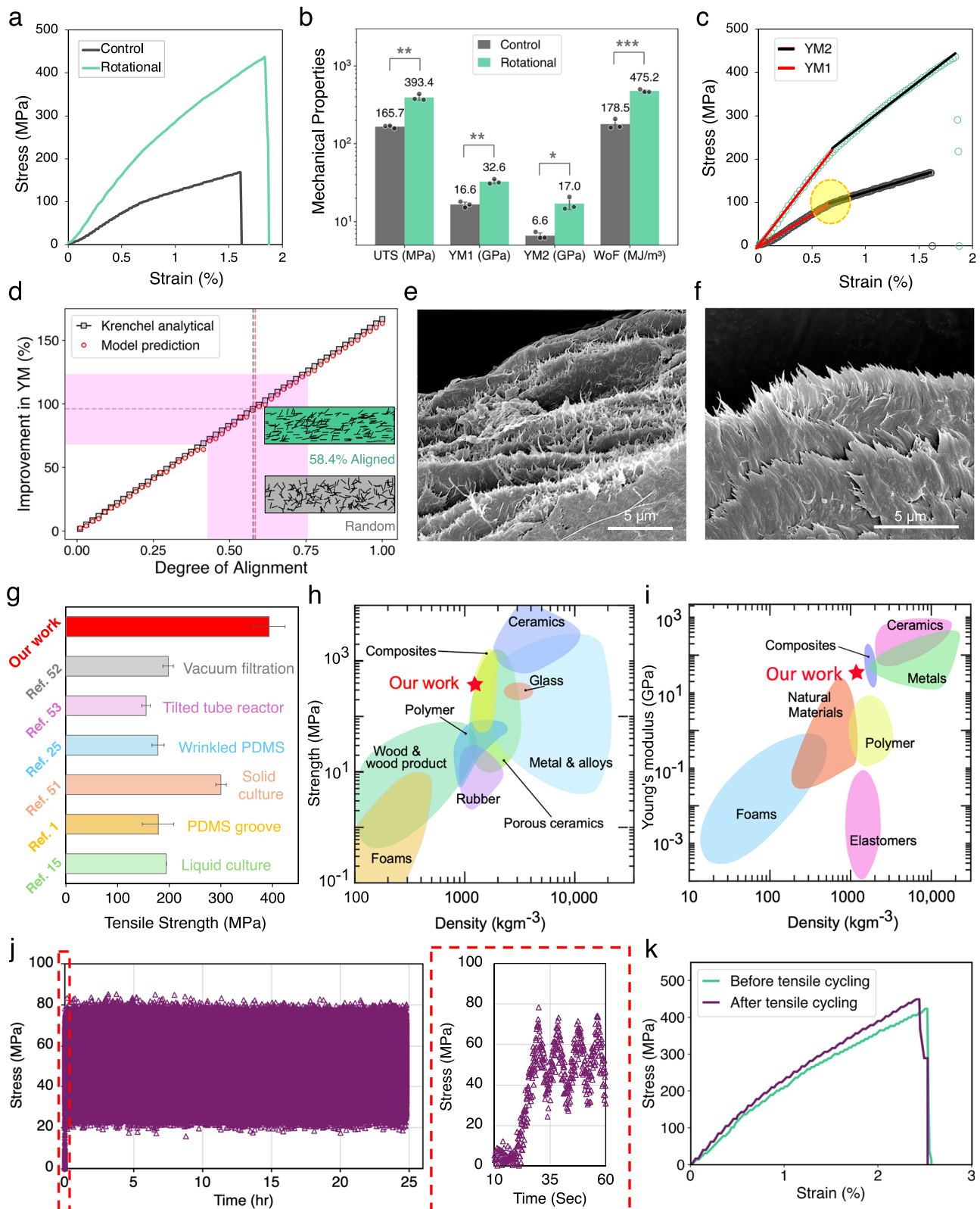


Fig. 2 | Alignment and morphological study of rotational device grown bacterial cellulose (BC) sheet. **a** Typical 2D wide-angle X-ray (WAX) scattering patterns for BC sheets from (i) static culture (control) and (iv) rotational culture. Intensity versus scattering vector q and azimuthal angle χ for (ii) control and (v) rotational culture, as labeled, within a q range of 1.1 to 1.36 \AA^{-1} . This range contains a strong equatorial diffraction peak of cellulose at $q = 1.25 \text{ \AA}^{-1}$ ($2\theta = 17.6^\circ$). (iii, vi) Two-dimensional fits to the corresponding data in (ii) and (v). From these fits, Herman's orientation parameters are obtained. **b** Representative SEM image of the BC sheet produced from (i) static culture device shows the random alignment of nanofibrils. Similar morphological features were consistently observed in three independently

repeated experiments. Inset. AFM image of the BC sheet produced from static culture. Representative SEM image of BC sheet from (ii) the rotational device shows increased alignment in the direction of rotation. Similar morphological features were consistently observed in three independently repeated experiments. Inset. AFM image of the BC sheet produced from rotational culture device. **c** Visualization under a polarized optical microscope of the BC sheet from (i–iii) static culture and (iv–vi) rotational device culture. The first column shows transmitted light, while the second and third column shows polarized light at 0° and 45° (incident polarized light beam vs sample orientation) respectively. Samples are circularly rotated within the same plane, perpendicularly to the incident polarized light beam.



hydrogen bonding (Supplementary Fig. 10). As more bonds break due to fiber sliding, rotational BC sheets can effectively dissipate more energy, thereby contributing to the enhanced WoF observed.

Next, we investigate the mechanistic effects of nanofibrillar alignment on the mechanical properties of the BC sheets and attempt to quantify the degree of alignment from a theoretical perspective. BC structures from static culture are assumed to have N number of fibrils

with a random uniform distribution, $N(\phi)$; while the relatively aligned samples from rotational culture have been modeled by a Weibull distribution, $N(X)$ with two parts. The proportion of fibers, X , that are aligned to the direction of tensile loading has been modeled by a Weibull distribution (shape parameter = 0.8), while the remaining fraction of fibers follows the random uniform distribution. (Supplementary Fig. 11). We apply a 5° tolerance to fibers' orientation,

Fig. 3 | Mechanical property characterization and performance comparison of BC sheet. **a** Typical tensile strain-stress curve for static (control) and rotational BC sheets. **b** Statistical comparison of ultimate tensile stress (UTS), Young's modulus (YM) and work of failure (WoF) of the BC sheets from static and rotational culture with the mean values noted atop. YM1 and YM2 represent the slopes of linear fits to the low-strain (<0.6%) and high-strain (>0.6%) regions, respectively. Bars represent mean values, and error bars indicate standard deviation ($n = 3$ independent samples per category). Statistical significance was determined using two-sided independent Welch's t-tests. Asterisks indicate significance levels: $p \leq 0.05$ (*), $p \leq 0.01$ (**), and $p \leq 0.001$ (***). Exact p values: UTS ($p = 0.00713$), YM1 ($p = 0.00118$), YM2 ($p = 0.0286$), and WoF ($p = 0.000148$). **c** Linear fittings to the strain-stress curve, shown in **(a)** for calculating YM1 (red line) and YM2 (black line). **d** Correlation between % improvement in YM and the degree of alignment using Krenchel analytical model (square symbol), our model prediction (circle symbol) and experimental data (pink shaded area). Inset shows two model BC sheets with 58.4%

alignment (green) and random alignment (grey). Representative SEM image the fractured surface of BC sheets from **(e)** static culture and **(f)** rotational culture. Compared to the static grown BC, rotational device grown BC shows directional alignment and more fiber pull-out. Similar morphological features were consistently observed in three independently repeated experiments. **g** Comparison of tensile strength across various single-step synthesis methods for BC. Bars represent mean values, and error bars indicate standard deviation. **h** Ashby plot of strength and density shows that the BC grown from rotational culture has higher strength than polymers and glass (indicated in red star). **i** Ashby plot of Young's modulus and density shows that BC (indicated in red star) has Young's modulus higher than most of the natural materials and even comparable to some metals. **j** Cyclic tensile loading (10,000 cycles) rotational BC at 50 ± 30 MPa. Inset shows zoomed-in (red dotted area) cyclic loading for first 1 min of the cycling depicting triangle-shaped loading input. **k** Tensile stress-strain curves of the rotational BC before and after 10,000 cycles of loading.

suggesting that our model recreates the BC structures with X fraction of fibers aligned to $(0 \pm 5)^\circ$ to the direction of loading.

Krenchel proposed the phenomenal theory of fiber-reinforced composites by modeling the efficiency factor of reinforcement, η as:

$$\eta = \sum_n a_n \cdot \cos^4 \varphi_n \quad (1)$$

Here, φ_n is the angle between the longitudinal direction of fibers and loading direction, and a_n is the proportion of fibers which are oriented at an angle φ_n . The basis of Krenchel's model is dividing all the fibers into groups of parallel fibers. Each of the members of the summed series, a_n , is thus equal to the particular group's proportion to the total fibers. According to Krenchel, for randomly aligned samples, $\eta = 3/8$, while that for perfectly aligned samples is 1⁴⁴. Using Krenchel's derivation and a simple rule of mixture (X fraction of fiber is perfectly aligned and $1-X$ fraction is randomly aligned), an analytical model can be established (the derivation is shown in Supplementary Information) as a relation between degree of alignment, X and percentage change of YM (% ΔYM):

$$\% \Delta YM = \left(\frac{5}{3} \times 100 \right) X \quad (2)$$

Due to the Hookean nature of the analysis, we investigated the elastic properties (YM) of our modeled BC sheets and predicted the % ΔYM as a function of X . To incorporate the effect of distribution of fibers/fiber alignment, we combine Krenchel's model with our model distributions, $N(X)$ and $N'(X)$:

$$\% \Delta YM = \frac{\sum_n \frac{N'(X)_n}{N} \cdot \cos^4 \varphi_n - \sum_n \frac{N(X)_n}{N} \cdot \cos^4 \varphi_n}{\sum_n \frac{N(X)_n}{N} \cdot \cos^4 \varphi_n} \quad (3)$$

At first, to validate the model distribution, we calculate the value of % ΔYM at specific X values as a function of N and find that $N = 5000$ brings the model prediction sufficiently close to the analytical model, indicating that the results are independent of N for $N > 5000$ (Supplementary Fig. 12). Note that the tensile cross-sectional area (width: 3 mm, avg thickness: ~25 microns) of the samples used in our experiment can accommodate nanofibers on the order of 10^8 (assuming fibril width ~ 50–100 nm and thickness ~ 4–10 nm). Therefore, $N = 5000$ significantly reduces the computational cost. Figure 3d shows that our model prediction converges with the Krenchel analytical relation. We

can use our model to estimate the fraction of fiber alignment, X , by comparing it with the experimental value of % ΔYM . The experimental % ΔYM is ~96%, which corresponds to $X_{\text{Krenchel analytical}} = 0.576$ and $X_{\text{Model prediction}} = 0.584$. Thus, according to our model, rotational BC has 58.4% of fibers aligned within $(0 \pm 5)^\circ$ of the loading direction. A model BC sheet with 58.4% alignment is shown in Fig. 3d inset. The pink band depicts the experimental standard deviation error and ranges from $X = 0.43$ to $X = 0.75$. Note that the HO factor determined from WAXS measurement (also ranges from 0 to 1) was ~0.489. Thus, the range of degree of alignment, predicted by our model, is close to the experimentally observed HO factor. The observed discrepancy might stem from the fact that the mechanical properties of BC sheets depend on several factors, e.g., fiber length, diameter, alignment, interfibrillar bonding, etc⁴⁴. However, not all these factors were considered in our model, and the % ΔYM was assumed to be a function of fiber alignment only. Nonetheless, our analysis provides a decent estimation of the degree of alignment of BC sheets obtained from rotational culture devices.

Figure 3e shows the cross-sectional image of the control BC film with a small number of pulled-out nanofibers and a porous layer-by-layer structure. Such a porous fracture surface suggests a weak hydrogen bonding between the randomly oriented fibrils, resulting in a low tensile strength¹⁵. On the contrary, the cross-sectional surface image of the rotational BC film (Fig. 3f) shows a large number of pulled-out cellulose nanofibers and a relatively denser fracture area. The fluid flow-assisted shear forces induce nanoscale alignment of the nanofibrils and form densely packed microfibril bundles, indicating the strong interaction (mainly refers to hydrogen bonding here) among the cellulose nanofibers. It is further supported by the calculated density comparison of the BC sheets (Supplementary Fig. 9). The density of the BC sample from the rotation culture device was 1361.1 ± 101.4 kg/m³, which was more compared to 966.9 ± 69.4 kg/m³ density of BC from static culture. This indicates that rotation culture flow improved the nanofibrillar packing in the cellulose network and formed a more compact structure. Based on the experimental density of BC samples, the porosity of each sample was calculated to be $40.3 \pm 4.3\%$ and $16.0 \pm 6.3\%$, for static and rotational BC sheets, respectively, using the theoretical density value of 1.62 g/cm³ of crystalline cellulose. Finally, the grammage of BC sheets from static (27.9 ± 4.9 g/m²) and rotational culture (27.2 ± 2.0 g/m²) were comparable, indicating that variations in grammage and/or coverage did not contribute to differences in the mechanical properties of BC. This

Table 1 | Mechanical properties of static and rotational BC

	UTS (MPa)	YM1 (GPa)	YM2 (GPa)	WoF (MJ/m ³)	Fracture strain (%)
Static BC	165.7 ± 5.9	16.6 ± 1.5	6.9 ± 0.7	178.5 ± 21.5	1.8 ± 0.2
Rotational BC	393.3 ± 30.5	32.6 ± 2.3	17.0 ± 3.3	475.2 ± 17.2	2.1 ± 0.1

is further corroborated by the observed differences in the mechanical properties of the BC sheets at two distinct grammage levels (Supplementary Fig. 13). At both low ($\sim 10 \text{ g/m}^2$) and high ($\sim 30 \text{ g/m}^2$) grammage levels, the rotational BC exhibited superior mechanical properties compared to the control samples. This suggests that the dominant factor contributing to enhanced mechanical performance in our system is the nanofibril alignment induced by the rotational biosynthesis process^{45,46}. Note that BC is a porous material, and the pore volume and density (thickness measurement can be easily underestimated or overestimated due to the unevenness of the surface) can be underestimated or overestimated. Therefore, instead of directly calculating the stress, i.e., force per unit area, a more realistic way is to use a specific stress or indexed stress (σ^w), which simply means a division of the force (F) by the width (b) and grammage (w) and then multiplying with the theoretical density ($\rho_{\text{theoretical}} = 1.62 \text{ g/cm}^3$). In this way, we obtained the stress ($\frac{F}{bw} \cdot \rho_{\text{theoretical}}$), which reflects the mechanical properties of the solid material regardless of the pore volume⁴⁷.

Fabricating anisotropic materials involves a tradeoff: while properties along the aligned direction are significantly enhanced, performance in the transverse direction is often compromised. However, this tradeoff can be strategically leveraged, as anisotropic materials offer unique advantages for both structural and functional applications⁴⁸. For example, fiber-reinforced composites with anisotropic fiber alignment are highly desirable for load-bearing applications and for optimizing directional properties like thermal or electrical conductivity^{49,50}. Similarly, the fibrillar alignment in our rotationally grown BC imparts anisotropic characteristics to the material (Supplementary Fig. 14). Note that despite this inherent anisotropy, the mechanical properties in the transverse direction (90°) are comparable to those of the control samples from static culture. Nonetheless, the anisotropic nature of the material requires careful consideration when tailoring properties for specific unidirectional applications.

We compared the mechanical properties of the BC sample from our rotational device to those of other existing methods. Due to improved nanofibrils alignment, the rotation culture device successfully yielded BC samples with higher tensile strength compared to other existing methods. For example, our rotationally cultured BC samples ($393.3 \pm 30.5 \text{ MPa}$) achieved more than 2 times as high tensile strength as BC produced from the wrinkled PDMS template ($\sim 178.1 \text{ MPa}$)²⁵. Another study that used a 3D-printed mold to grow aligned BC achieved $\sim 260.4 \text{ MPa}$ tensile strength after 20% post-harvest stretching, which is still lower than our rotational culture-grown BC¹. So far, our rotational BC demonstrated the highest tensile strength among all reported values for BC harvested directly from the culture in a single step^{1,15,25,51–53} (Fig. 3g). Note that in our work, BC samples were not post-processed (e.g., stretched), thus eliminating the need for additional stretching machinery, time, effort, and costs of the post-processing and circumvents the risk of sample tearing during alignment by stretching. As a result, we did not compare our rotational BC with those using post-harvest processing. Nonetheless, we envisage that with continued refinement of our engineered biosynthesis process, the properties of our BC can be further improved. We positioned our BC sheet against different synthetic materials, metal/alloys, natural materials, composites, etc., to strength or Young's modulus vs. density in the Ashby plot (Fig. 3h, i). We observe that the mechanical strength of our BC sheet exceeds many important classes of materials, including polymers and a majority of metals, alloys, and glass. Young's modulus of our BC sheet is higher than all polymers, almost all natural materials, and in the range of metals and composites while being lightweight. Thus, this material can be suitable for different applications⁵⁴, such as structural, textile, green electronics, etc.

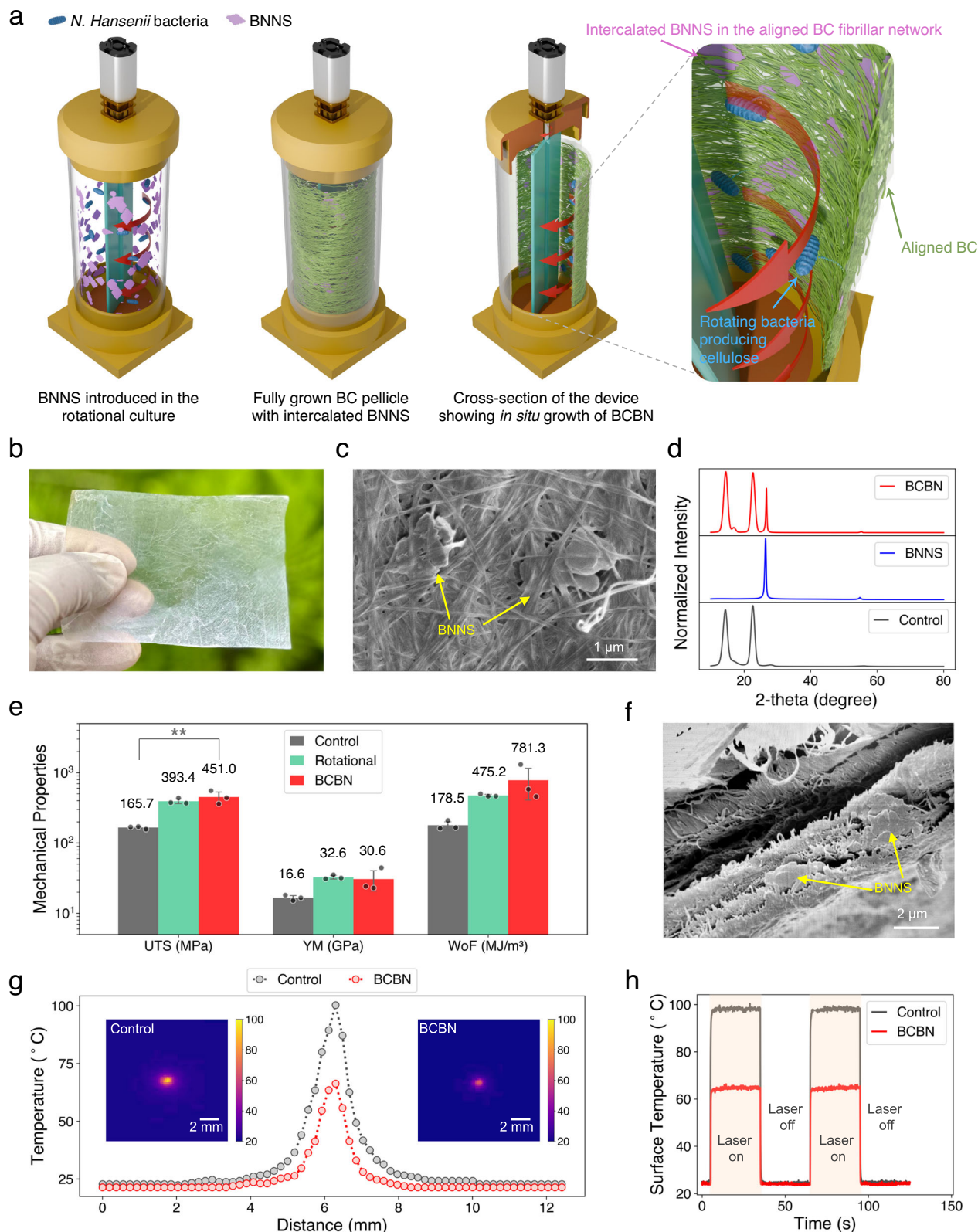
In addition to high mechanical strength and stiffness, the rotational BC exhibits fatigue resistance, which is important to maintain stable mechanical properties during long-term use⁵⁵. To further

explore the applicability of our rotational BC in practical settings, cyclic tensile tests were systematically carried out in which samples experienced cyclic (triangular-shaped input) loading at $50 \pm 30 \text{ MPa}$ (Supplementary Fig. 15). This corresponds to $13 \pm 8\%$ of the average UTS (393.3 MPa) of rotational BC. Remarkably, after 10,000 loading cycles, the tensile behavior of the rotational BC remained almost unchanged (Fig. 3j). Moreover, the sample surface, after the aggressive cyclic tensile loading, did not show any sign of structural damage while maintaining the compactness and nanofibrillar alignment (Supplementary Fig. 16), highlighting the robustness of its 3D network structure. This mechanical stability was further confirmed by the nearly identical stress-strain curves recorded before and after the cyclic tests (Fig. 3k). Additionally, the UTS of rotational BC after 10,000 cycles was approximately 440 MPa —about $\sim 166\%$ higher than the average UTS of control BC—demonstrating its superior durability under complex loading conditions.

Robust multifunctional bacterial cellulose-hexagonal boron nitride hybrid sheet

Limited diffusion of nanoscale building blocks from the liquid medium to the upper surface layers of newly grown BC³³ and dispersion stability of the nanomaterials in a static environment throttles the realization of robust multifunctional BC-based hybrid systems (Supplementary Fig. 17). However, our rotational culture method offers the advantage of seamless and homogeneous integration of nanoscale building blocks into the aligned BC network by simply adding the nanoscale additives in the nutrient media (Fig. 4a). Moreover, the moving rotor provides dispersion/colloidal stability to the nanoparticles via its continuous motion. As the nanoscale model system, we chose hexagonal boron nitride (hBN) nanosheets (BNNS), a promising two-dimensional (2D) inorganic nanomaterial with excellent mechanical properties (Young's modulus $\sim 0.8 \text{ TPa}$), thermal properties (thermal conductivity $\sim 300\text{--}2000 \text{ Wm}^{-1} \text{ K}^{-1}$) and biocompatibility⁵⁶. After the incubation period, the tubular sheet of bacterial cellulose-hexagonal boron nitride (BCBN) hydrogel was harvested from the device and dried overnight to obtain a flat, homogeneous, transparent, and flexible BCBN sheet (Fig. 4b and Supplementary Fig. 18) with an average thickness of $\sim 10 \mu\text{m}$. Morphological investigation of the film under a high-resolution SEM reveals encapsulated 2D BNNS within the 1D BC nanofibrillar network, thus resulting in a hierarchical 1D–2D hybrid nanosheet (Fig. 4c, Supplementary Fig. 19) with uniformly distributed BNNS (Supplementary Figs. 19 and 20). Note that while those BNNS buried within the BC network are fully encompassed by the nanofibrils, those on the surface remain partially exposed and thus appear slightly coarse, especially around the edges. This is a natural outcome of the dynamic biosynthesis process, where the BNNS becomes physically entangled on the surface of the BC nanofibrillar network and does not get fully enclosed by the subsequent BC layer. This can also be attributed to the size difference between the BNNS, which are on average $1 \mu\text{m}$ in lateral width, and the BC nanofibrils, which are on the order of nanometers. Nonetheless, full enclosure of BNNS and spatial locking caused by entanglements of BC fibrils occurs within the bulk of the network.

The presence of both BC and BNNS in the BCBN hybrid nanosheet is confirmed by X-ray diffraction (XRD) (Fig. 4d). Specifically, the hybrid nanosheet retains the broad peak of BC at 14.4 and 22.7° and a minor peak at 16.8° , corresponding to the diffractions of ($\bar{1}10$), (200), and (110) planes of cellulose I, respectively⁵⁷. Additionally, the XRD peaks corresponding to the (002) and (004) planes of BNNS indicate the BNNS structure is well-preserved in the BCBN hybrid nanosheet. Interestingly, the BNNS diffraction peak slightly shifts from 26.65° for pristine BNNS to 26.70° for BCBN, which corresponds to a decrease in d-spacing from 3.342 \AA to 3.336 \AA and may be associated with the stacking process of the BNNS in the BC network under the shear force of the rotational culture. Further, the disappearance of all other peaks



except (002) and (004) peaks in BCBN suggests that the (001) plane of BNNS is oriented parallel to the face of the hybrid nanosheet.

Thermogravimetric analysis (TGA) reveals that the thermal stability and decomposition behavior of the BCBN hybrid nanosheet improved throughout the whole range of temperatures upon the addition of BNNS in the BC network (Supplementary Fig. 21). Specifically, the BCBN hybrid nanosheet exhibited excellent thermal stability

up to 300 °C, compared to 275 °C for the control BC. As the temperature increases, BNNS continues to inhibit the decomposition of the polymers by transferring the heat mostly through the BNNS. At higher temperatures above 500 °C, BCBN demonstrates more residual weight compared to BC due to the higher thermal stability of BNNS. The TGA analysis determined the wt% of BNNS in the BCBN hybrid nanosheet to be around 5–6%.

Fig. 4 | Biosynthesis, characterization and performance evaluation of bacterial cellulose-hexagonal boron nitride (BCBN) hybrid nanosheets. **a** Schematic of the biosynthesis process for growing in situ BCBN hybrid nanosheet using our rotational culture device. The partially enlarged schematic on the right shows boron nitride nanosheet (BNNS) diffusion in the shear flow and its intercalation in the fibrous BC network. **b** Optical photograph of the dried BCBN hybrid nanosheet. **c** Representative SEM image of BCBN showing intercalated BNNS within the BC network. Similar features were consistently observed across multiple regions of the same sample. **d** XRD comparison of BC, BNNS, and BCBN. **e** Statistical comparison of UTS, YM, and WoF of the BC sheets from static culture, rotational culture, and BCBN from rotational culture with the mean values noted atop. Bars represent

mean values, and error bars indicate standard deviation ($n = 3$ independent samples per category). Statistical significance was assessed using two-sided one-way ANOVA. The double asterisk (**) denotes a statistically significant difference among the groups ($p \leq 0.01$). p value for UTS is 0.0025. **f** Representative cross-section SEM image of the fracture surface of BCBN film shows both BC and BN pull-out. Similar features were consistently observed across multiple regions of the same sample. **g** Comparison of single line temperature profile from temperature mapping of BC and BCBN using IR camera under 25-mW laser illumination in air. The temperature profile shows higher temperature for BC compared to BCBN. Inset shows thermal mapping of control (left) and BCBN (right) samples under laser illumination. **h** Temporal heat dissipation behavior of BC and BCBN.

The mechanical performance of the BCBN sheets produced by the rotational device was evaluated by uniaxial tensile testing and compared with the BC sheets from static and rotational cultures. Figure 4f shows the statistical comparison of UTS, YM, and WoF of the samples with standard deviation, and Supplementary Fig. 22 shows a representative and comparative stress-strain plot of BCBN. The average tensile strength of the rotational BCBN sheets increased by -172 % (from 165.7 ± 5.9 MPa to 451.0 ± 79.0 MPa) than static BC and by -15% (from 393.3 ± 30.5 MPa to 451.0 ± 79.0 MPa) than rotational BC. The average YM of the BCBN was found to be -84% higher than that of static BC (from 16.6 ± 1.5 GPa to 30.6 ± 12.0 GPa), while not showing improvement compared to the BC grown from rotational device (from 32.6 ± 2.3 GPa). Note that the YM is determined from the initial linear region of the stress-strain plot and, hence, can depend on the interface of BC and BNNS. Therefore, the discrepancy might stem from the discontinuous and non-engineered interface of BC and BNNS (BNNS are known to possess exceptional chemical stability). The average WoF of the BCBN sheets increased by -338% (from 178.5 ± 21.5 MJ/m³ to 781.3 ± 374.0 MJ/m³) and -64% (from 475.2 ± 17.2 MJ/m³ to 781.3 ± 374.0 MJ/m³) compared to that of static and rotational BC respectively. Evidently, with the incorporation of BNNS, the strength and toughness (WoF) improved, suggesting the simultaneous strengthening and toughening effect of BNNS. The observed difference in the mechanical properties is due to (1) the physical intercalation of the 2D BNNS and 1D BC nanofibril and (2) the effective distribution of BNNS in the BC network. During the tensile stretching process, the nanofibrils are stretched, followed by slippage between adjacent fibrils. The presence of BNNS physically resists the sliding of the nanofibrils, resulting in the stress being uniformly dispersed in the BCBN network⁵⁸. Consequently, fiber pull-out and BNNS pull-out could be observed from the cross-sectional SEM image of the BCBN hybrid (Fig. 4g).

Next, we investigated the thermal properties of BCBN. To understand the thermal behavior, the steady-state heating of BC and BCBN under illumination by a white supercontinuum laser was studied using high-resolution spatial and temporal mapping of temperature variations with a thermal infrared (IR) camera^{59,60}. As shown in Fig. 4h, the induced heat for BC was found to be concentrated with high intensity compared to BCBN, which demonstrates a rather diffused circle with low intensity. This indicates better heat transfer/dissipation behavior of BCBN. The single-line temperature profiles were extracted from temperature mapping captured by the IR camera and analyzed (Fig. 4h). When illuminated with a laser of the same power, the line profile of BC showed higher peak temperature (maximum surface temperature -100.34 °C) and a broader full-width half maximum (FWHM) than those of BCBN (maximum surface temperature -60.3 °C). The significantly low surface temperature of the hybrid nanosheet indicates an improved thermal conductivity and/or heat transfer rate, thereby homogenizing the heat generated by the laser. At the same time, the narrow FWHM suggests complete heat dissipation within a very short range. To observe the time-dependent heat dissipation behavior, temporal changes in the maximum surface temperature are also recorded, which shows better performance for BCBN

(Fig. 4i). Specifically, under a given illumination power, BCBN exhibits a significantly faster thermal response, compared to BC, to reach the expected steady-state surface temperature. We also calculated the rate of heat dissipation from the temporal mapping of the surface temperature variations after the illumination ceased. Both BC and BCBN showed a third-order temperature decay, with a three times higher calculated decay rate for the BCBN hybrid nanosheet (Supplementary Fig. 23).

Overall, the rotational culture device offers several advantages over traditional static culture while being sustainable and scalable (Supplementary Fig. 24). The flow-assisted shear-aligned BC has proven to be mechanically stronger than the static BC sheets. In this regard, the rotational BC shows improvement in both strength and toughness, which are traditionally deemed as mutually exclusive properties. Moreover, the freedom of developing robust BC-based hybrid nanosheets by simply adding nanoscale additives to the nutrient media underpins the efficacy of our dynamic biosynthesis approach. When compared to BC reinforced with other nanosheets reported in the literature, such as graphene, nanoclay, carbon nanotubes (CNTs), etc., our BCBN exhibits markedly superior performance in both strength and stiffness (Supplementary Fig. 25 and Supplementary Table 1). In theory, this approach holds the potential for incorporating different nanoscale building blocks in the BC network, thus enabling on-demand tuning of functionalities. However, this remains a subject for future research to experimentally validate and demonstrate its feasibility. Nonetheless, we envision the robust multifunctional BCBN hybrid nanosheet synthesized using our method, finding potential use in advanced applications such as green electronics, thermal management, and energy storage.

In summary, we report a simple, one-step method to produce strong BC by aligning nanofibrils in situ using directional media flow in a custom-designed rotation culture device. The high alignment of nanofibrils in the BC produced in this study resulted in mechanical properties comparable to strong materials such as metals and glasses while maintaining superb flexibility, foldability, lightweight, and eco-friendliness. This is obtained in a single processing step, reducing additional machinery, time, and cost because the rotational culture device is simple, inexpensive, scalable, and can be built upon existing chemical incubators. We also demonstrate the versatility of the method by developing robust BC-based hybrid nanosheets with nanoscale building blocks uniformly distributed in the nanofibrous network of BC. Our dynamic process enabled us to combine the unique properties of BC and BNNS, resulting in improved characteristics and multifunctionalities that surpass those of the individual components. We envisage our aligned, strong, and multifunctional BC sheets will pave the way towards a wide range of practical applications.

Methods

Design and 3D printing of rotational culture device

The rotational culture device consisted of five parts: a base, cap, shaft (width: 20 mm, thickness: 3 mm, and length: 90 mm), PDMS tube (inner diameter, ID: 36 mm, outer diameter, OD: 38 mm, and length: 90 mm), and DC motor (60 RPM 6 V). The dimension of the base was

fixed such that the tube was firmly fixed to the base and did not lead to any fluid leak from the system. The cap is an essential component that enables the connection between the DC motor and the agitator through a hole acting as a bridge. The DC motor is a single-speed brushless motor powered by a 6 V power supply. The dimensions of the individual parts are depicted in Supplementary Fig. 3. The individual parts of the rotational culture device (base, cap, and shaft) were 3D-printed using a Formlabs stereolithography (SLA) printer (Form 2, USA) with a 405 nm laser source. The parts were printed with gray photopolymer resin (Formlabs Gray Resin V4 1 L, USA). After printing, all parts were separated from the substrate, washed in isopropanol (IPA) for 5 min to remove excess resin, and then air-dried. The air-dried parts were UV-cured at 50 °C for 20 min.

Frozen stock preparation of cellulose-producing bacteria

Novacetimonas hansenii NQ5 ATCC 53582 (formerly *Komagataeibacter* and *Gluconacetobacter*) lyophilized cells were obtained from the American Type Culture Collection (ATCC). The cells were resuspended in 0.5 mL Hestrin-Schramm (HS) broth. HS broth was prepared using 20 g glucose, 5 g yeast extract, 5 g casein tryptone, 1.5 g citric acid monohydrate, and 10.8 g disodium phosphate in 1 L ultrapure water adjusted to pH 5.5 using NaOH. A portion of the resuspended broth was streaked on HS agar to screen for opaque cellulose-producing (Cel⁺) colonies. HS agar was prepared by adding 15 g/L agar to the HS broth, followed by pouring in 100 mm Petri dishes, dried for 24 h and stored at 4 °C in tightly sealed bags. One of the colonies from the HS agar was dispersed in 2 mL HS broth supplemented with 2% V/V cellulase (Sigma C2730) to inhibit pellicle formation. It was then grown in a culture tube by shaking at 200 rpm, 30 °C, 24 h, before mixing with equal volume 50% V/V glycerol and then stored at –80 °C as a frozen cell stock.

Preparation of boron nitride nanosheets

8 g of commercial hBN micro-powder (~30 microns, Lower Friction Lubricants, MK Impex Corp.) was dispersed in isopropyl alcohol (IPA) (2 L, purity ≥99.5%). The dispersion was sonicated in an iced sonic bath for 48 h and then centrifuged at 771 × g for 20 min. After centrifugation of the dispersions, the supernatant was decanted, and the supernatant was then filtered via vacuum filtration. After filtration, a BN cake was obtained, which was dried for 4 h in an oven at 60 °C. The dried BNNS powder was used as the secondary inorganic phase for the hybrid nanosheets after grinding using a ceramic mortar-pastel. The exfoliated BNNS had an average lateral size of 1 μm and thickness of 3–4 nm.

Bacterial cellulose and bacterial cellulose-hexagonal boron nitride sheet production

To prepare for bacterial cellulose (BC) growth, frozen cell stock was scraped and streaked onto HS agar plates, then incubated at 30 °C for 3–4 days until colonies approximately 1–2 mm in diameter formed. Several colonies were picked and dispersed into HS broth supplemented with 2% V/V cellulase and precultured by shaking at 200 rpm and 30 °C for 48 h. The resulting culture was centrifuged at 2000 × g for 5 min, and the pellet was washed once with an equal volume of 10% glycerol to remove residual cellulase before being resuspended in fresh HS broth. The optical density (OD₆₀₀) of the washed cell suspension was measured using a Thermo Scientific NanoDrop spectrophotometer. Fresh HS broth was inoculated with an appropriate volume of the cell suspension to achieve an OD of ~0.015.

For static cultures, 50 mL of the inoculated broth was transferred into 250 mL Erlenmeyer flasks. For rotational cultures, 65 mL of the inoculated broth was loaded into UV-sterilized rotational culture devices, prepared inside a laminar flow hood. The rotation devices, equipped with DC motors wired through a breadboard and connected to an AC power supply, were operated inside an incubator at 30 °C for 10 days.

After incubation, BC sheets were harvested from the inner surface of the PDMS tubing using a spatula and transferred to 100 mm Petri dishes. The sheets were treated with 0.5 M NaOH at 90 °C for 20 min to remove bacterial residues, then thoroughly washed with deionized (DI) water until the pH reached 7.0. Finally, the BC sheets were dried at room temperature by sandwiching them between two Whatman filter papers. BC-BN composite sheets were prepared following the same procedure, with the addition of 150 mg of boron nitride nanosheets (BNNS) to the culture medium during inoculation.

Characterizations

Mechanical testing (uniaxial tensile test) was performed on an ARES G2 Rheometer (TA Instruments). Rectangular specimens of ~3 mm width and ~30 mm length were tested at a gauge length of 10 mm and a crosshead speed of 5 mm min^{–1}. At least three samples were tested for each category. The dried BC sample was sandwiched between two paper cards to avoid sample damage and/or slippage during tensile testing. Supplementary Fig. 24 depicts the steps involved and relevant dimensions used for the testing. The weight was measured using a microbalance, and sample density was calculated using weight divided by volume. Cyclic tensile tests were systematically carried out using Instron ElectroPuls E3000. Rectangular specimens of ~3 mm width and ~30 mm length were tested at a gauge length of 10 mm and a crosshead speed of 0.2 mm min^{–1} with cyclic (triangular-shaped input) loading at 50 ± 30 MPa (Details can be found in Supplementary Fig. 15).

Wide-angle X-ray scattering (WAXS) was performed using Xeuss 3.0 (Xenocs). The X-ray wavelength was 1.54 Å, the sample-to-detector distance was 55 mm, and the exposure time was 30 min. Samples were taped directly to a sample holder so that no substrate or capillary was needed. A Pilatus3 300k detector was used to collect scattered X-rays. Raw two-dimensional scattering patterns were converted to intensity versus scattering vector q and azimuthal angle χ using the pyFAI Python library. This data was then fitted in two dimensions using the SciPy curve_fit Python library. The peak was fitted with a Gaussian line shape in q and a Poisson distribution in χ , as well as a linearly varying background ($I = aq + b$).

Scanning Electron Microscopy (SEM) was performed using a FEI Helios NanoLab 660 SEM/FIB. Dried BC samples were coated with 10 nm thick of gold using a Denton Desk V Sputter system. The samples were imaged with 5 kV at different magnifications. Elemental mapping was performed using a FEI Helios SEM/FIB instrument. Atomic force microscopy (AFM) images were obtained using a Park NX-20 microscope in tapping mode. The measurements were conducted in the air using AC160TS-R3 cantilevers (Oxford instruments) at room temperature. Optical/light microscopy was performed with a Zeiss Axio-plan 2 microscope equipped with a Zeiss AxioCam 208 camera. Each set of polarized optical microscopic (POM) images received the same contrast adjustments. All images for this analysis were taken using the same microscope illumination settings.

Thermogravimetric analysis (TGA) was performed using a Mettler Toledo TGA/DSC 3+ system. Samples were placed in alumina pans and heated from 25 °C to 900 °C at a rate of 10 °C min^{–1} under a nitrogen atmosphere.

X-ray diffraction (XRD) measurements were conducted using a Rigaku SmartLab diffractometer with Cu K α_1 radiation ($\lambda = 0.154$ nm). Diffraction patterns were collected over a 2θ range of 20° to 90°, with a scan rate of 10° min^{–1} and a step size of 0.01°.

An in-situ thermal imaging was conducted to monitor the surface temperature measurements using a FLIR A615 infrared camera. The heating of samples was achieved by irradiating them with a super-continuum laser source (Fianium, 485–700 nm, 78 MHz), which was focused onto the sample surface through a 75 mm focal length lens, producing an illumination area of approximately 1.5 mm². A neutral density filter (Thorlabs, NDC-100C-4M) was used ensuring a constant illumination power of 25 mW during testing. For measurement

consistency, samples were positioned on an inverted glass petri dish (93 mm diameter) placed atop an optical table. The laser beam was oriented perpendicularly to the sample surface, while the IR camera was fixed at a 25° observation angle relative to the beam axis. Prior to data acquisition, the camera focus was carefully optimized and maintained throughout the experiment. Thermal images of the illuminated samples were then collected using the IR camera. For time-dependent thermal response analysis, we monitored the maximum surface temperature as a function of time during both the heating phase (30 s of continuous illumination) and the subsequent cooling phase (30 s after the laser was blocked).

Reporting summary

Further information on research design is available in the Nature Portfolio Reporting Summary linked to this article.

Data availability

All data needed to evaluate the conclusions in the paper are present in the paper and/or the Supplementary Information. All data underlying the study are available from the corresponding author upon request.

References

- Rahman, M. M. & Netravali, A. N. Aligned bacterial cellulose arrays as 'Green' nanofibers for composite materials. *ACS Macro. Lett.* **5**, 1070–1074 (2016).
- Mittal, N. et al. Multiscale control of nanocellulose assembly: transferring remarkable nanoscale fibril mechanics to macroscale fibers. *ACS Nano* **12**, 6378–6388 (2018).
- Das, P. P. & Chaudhary, V. Moving towards the era of bio fibre based polymer composites. *Clean. Eng. Technol.* **4**, 100182 (2021).
- Yang, H.-B. et al. Edible, ultrastrong, and microplastic-free bacterial cellulose-based straws by biosynthesis. *Adv. Function. Mater.* **32**, 211713 (2021).
- Lu, Y., Mehling, M., Huan, S., Bai, L. & Rojas, O. J. Biofabrication with microbial cellulose: from bioadaptive designs to living materials. *Chem. Soc. Rev.* **53**, 7363–7391 (2024).
- Wu, Z. et al. Insights into hierarchical structure–property–application relationships of advanced bacterial cellulose materials. *Adv. Funct. Mater.* **33**, 2214327 (2023).
- Gao, H.-L. et al. Bioinspired hierarchical helical nanocomposite macrofibers based on bacterial cellulose nanofibers. *Natl. Sci. Rev.* **7**, 73–83 (2020).
- Zhong, C. Industrial-scale production and applications of bacterial cellulose. *Front. Bioeng. Biotechnol.* **8**, 1425 (2020).
- Lin, S.-P. et al. Biosynthesis, production and applications of bacterial cellulose. *Cellulose* **20**, 2191–2219 (2013).
- Moniri, M. et al. Production and status of bacterial cellulose in biomedical engineering. *Nanomaterials* **7**, 257 (2017).
- Gomes, N. O., Carrilho, E., Machado, S. A. S. & Sgobbi, L. F. Bacterial cellulose-based electrochemical sensing platform: a smart material for miniaturized biosensors. *Electrochim. Acta* **349**, 136341 (2020).
- Torres, F. G., Troncoso, O. P., Gonzales, K. N., Sari, R. M. & Gea, S. Bacterial cellulose-based biosensors. *Med. Devices Sens.* **3**, e10102 (2020).
- Inácio, P. M. C. et al. Ultra-low noise PEDOT:PSS electrodes on bacterial cellulose: a sensor to access bioelectrical signals in non-electrogenic cells. *Org. Electron.* **85**, 105882 (2020).
- Wan, Y. et al. Scalable synthesis of robust and stretchable composite wound dressings by dispersing silver nanowires in continuous bacterial cellulose. *Compos. Part B: Eng.* **199**, 108259 (2020).
- Wang, S. et al. Transparent, anisotropic biofilm with aligned bacterial cellulose nanofibers. *Adv. Funct. Mater.* **28**, 1707491 (2018).
- Dugan, J. M., Gough, J. E. & Eichhorn, S. J. Bacterial cellulose scaffolds and cellulose nanowhiskers for tissue engineering. *Nanomedicine* **8**, 287–298 (2013).
- Hirayama, K. et al. Cellular building unit integrated with microstrand-shaped bacterial cellulose. *Biomaterials* **34**, 2421–2427 (2013).
- Yano, H. et al. Optically transparent composites reinforced with networks of bacterial nanofibers. *Adv. Mater.* **17**, 153–155 (2005).
- Huang, Y. et al. Recent advances in bacterial cellulose. *Cellulose* **21**, 1–30 (2014).
- Saito, T., Kuramae, R., Wohler, J., Berglund, L. A. & Isogai, A. An Ultrastrong nanofibrillar biomaterial: the strength of single cellulose nanofibrils revealed via sonication-induced fragmentation. *Biomacromolecules* **14**, 248–253 (2013).
- Wang, S. et al. Super-strong, super-stiff macrofibers with aligned, long bacterial cellulose nanofibers. *Adv. Mater.* **29**, 1702498 (2017).
- Putra, A. et al. Production of bacterial cellulose with well oriented fibril on PDMS substrate. *Polym. J.* **40**, 137–142 (2008).
- Putra, A., Kakugo, A., Furukawa, H., Gong, J. P. & Osada, Y. Tubular bacterial cellulose gel with oriented fibrils on the curved surface. *Polymer* **49**, 1885–1891 (2008).
- Sano, M. B., Rojas, A. D., Gatenholm, P. & Davalos, R. V. Electro-magnetically controlled biological assembly of aligned bacterial cellulose nanofibers. *Ann. Biomed. Eng.* **38**, 2475–2484 (2010).
- Prathapan, R. et al. In situ alignment of bacterial cellulose using wrinkling. *ACS Appl. Bio Mater.* **3**, 7898–7907 (2020).
- Chae, I. Shear-induced unidirectional deposition of bacterial cellulose microfibrils using rising bubble stream cultivation. *Carbohydrate Polymers* **255**, 117328 (2021).
- Benziman, M., Haigler, C. H., Brown, R. M., White, A. R. & Cooper, K. M. Cellulose biogenesis: polymerization and crystallization are coupled processes in *Acetobacter xylinum*. *Proc. Natl. Acad. Sci. USA* **77**, 6678–6682 (1980).
- Hsieh, Y.-C., Yano, H., Nogi, M. & Eichhorn, S. J. An estimation of the Young's modulus of bacterial cellulose filaments. *Cellulose* **15**, 507–513 (2008).
- Nakagaito, A. N., Iwamoto, S. & Yano, H. Bacterial cellulose: the ultimate nano-scalar cellulose morphology for the production of high-strength composites. *Appl. Phys. A* **80**, 93–97 (2005).
- Santmarti, A., Zhang, H., Lappalainen, T. & Lee, K.-Y. Cellulose nanocomposites reinforced with bacterial cellulose sheets prepared from pristine and disintegrated pellicle. *Compos. Part A: Appl. Sci. Manuf.* **130**, 105766 (2020).
- Shah, N., Ul-Islam, M., Khattak, W. A. & Park, J. K. Overview of bacterial cellulose composites: a multipurpose advanced material. *Carbohydr. Polym.* **98**, 1585–1598 (2013).
- Jiao, S., Zhou, A., Wu, M. & Hu, H. Kirigami patterning of mxene/bacterial cellulose composite paper for all-solid-state stretchable micro-supercapacitor arrays. *Adv. Sci.* **6**, 1900529 (2019).
- Guan, Q.-F. et al. A general aerosol-assisted biosynthesis of functional bulk nanocomposites. *Natl. Sci. Rev.* **6**, 64–73 (2019).
- Wan, Y. et al. Ultrathin, strong, and highly flexible Ti₃C₂T_x MXene/bacterial cellulose composite films for high-performance electromagnetic interference shielding. *ACS Nano* **15**, 8439–8449 (2021).
- Yamada, Y. et al. Description of Komagataibacter gen. nov., with proposals of new combinations (Acetobacteraceae). *J. Gen. Appl. Microbiol.* **58**, 397–404 (2012).
- Ruka, D. R., Simon, G. P. & Dean, K. M. Altering the growth conditions of *Gluconacetobacter xylinus* to maximize the yield of bacterial cellulose. *Carbohydr. Polym.* **89**, 613–622 (2012).
- Ashiotis, G. et al. The fast azimuthal integration Python library: pyFAI. *J. Appl. Crystallogr.* **48**, 510–519 (2015).
- Burger, C., Hsiao, B. S. & Chu, B. Preferred orientation in polymer fiber scattering. *Polym. Rev.* **50**, 91–111 (2010).
- Virtanen, P. et al. SciPy 1.0: fundamental algorithms for scientific computing in Python. *Nat. Methods* **17**, 261–272 (2020).
- Murugarren, N. et al. Highly aligned bacterial nanocellulose films obtained during static biosynthesis in a reproducible and straightforward approach. *Adv. Sci.* **9**, 2201947 (2022).

41. Henriksson, M., Berglund, L. A., Isaksson, P., Lindström, T. & Nishino, T. Cellulose nanopaper structures of high toughness. *Biomacromolecules* **9**, 1579–1585 (2008).
42. Ritchie, R. O. The conflicts between strength and toughness. *Nat. Mater.* **10**, 817–822 (2011).
43. Zhu, H. et al. Anomalous scaling law of strength and toughness of cellulose nanopaper. *Proc. Natl. Acad. Sci. USA* **112**, 8971–8976 (2015).
44. Krenchel, H. *Fibre Reinforcement: Theoretical and Practical Investigations of the Elasticity and Strength of Fibre-Reinforced Materials*. (Akademisk forlag, 1964).
45. Kontturi, K. S. et al. Influence of biological origin on the tensile properties of cellulose nanopapers. *Cellulose* **28**, 6619–6628 (2021).
46. l'Anson, S. J., Sampson, W. W. & Savani, S. Density dependent influence of grammage on tensile properties of handsheets. *J. Pulp Pap. Sci.* **34**, 182–189 (2008).
47. Ek, M., Gellerstedt, G. & Henriksson, G. (eds.) *Pulp and Paper Chemistry and Technology. Volume 4: Paper Products Physics and Technology*. (De Gruyter, Berlin, 2009).
48. Liu, Z., Zhang, Z. & Ritchie, R. O. Structural orientation and anisotropy in biological materials: functional designs and mechanics. *Adv. Funct. Mater.* **30**, 1908121 (2020).
49. Barile, C., Casavola, C. & De Cillis, F. Mechanical comparison of new composite materials for aerospace applications. *Compos. Part B: Eng.* **162**, 122–128 (2019).
50. Tian, T. & Cole, K. D. Anisotropic thermal conductivity measurement of carbon-fiber/epoxy composite materials. *Int. J. Heat. Mass Transf.* **55**, 6530–6537 (2012).
51. Sun, W. et al. Nacre-inspired bacterial cellulose/Mica nanopaper with excellent mechanical and electrical insulating properties by biosynthesis. *Adv. Mater.* **35**, 2300241 (2023).
52. Feng, Y., Zhang, X., Shen, Y., Yoshino, K. & Feng, W. A mechanically strong, flexible and conductive film based on bacterial cellulose/graphene nanocomposite. *Carbohydr. Polym.* **87**, 644–649 (2012).
53. Rahman, M. M. & Netravali, A. N. High-performance green nanocomposites using aligned bacterial cellulose and soy protein. *Compos. Sci. Technol.* **146**, 183–190 (2017).
54. Strength - Density. http://www-materials.eng.cam.ac.uk/mpsite/interactive_charts/strength-density/NS6Chart.html.
55. Ling, Z.-C. et al. Ultrastrong and fatigue-resistant bioinspired conductive fibers via the in situ biosynthesis of bacterial cellulose. *NPG Asia Mater.* **15**, 19 (2023).
56. Roy, S. et al. Structure, properties and applications of two-dimensional hexagonal boron nitride. *Adv. Mater.* **33**, 2101589 (2021).
57. Salem, K. S. et al. Comparison and assessment of methods for cellulose crystallinity determination. *Chem. Soc. Rev.* **52**, 6417–6446 (2023).
58. Shahzadi, K. et al. Bio-based artificial nacre with excellent mechanical and barrier properties realized by a facile in situ reduction and cross-linking reaction. *ACS Nano* **11**, 325–334 (2017).
59. Saadi, M. A. S. R. et al. Sustainable valorization of asphaltenes via flash joule heating. *Sci. Adv.* **8**, eadd3555 (2022).
60. Rahman, M. M. et al. Fiber reinforced layered dielectric nanocomposite. *Adv. Funct. Mater.* **29**, 1900056 (2019).

Acknowledgements

M.M.R. acknowledges the funding support from the National Science Foundation (award no. 2234567, M.M.R.) and U.S. Endowment for

Forestry and Communities, Inc. (Grant no. 23-JV-1111129-042, M.M.R.). M. P. acknowledges financial support from the Welch Foundation, grant C-1668. The authors thank Mario Norton from Rice University's Office of Research Development for helping with the 3D schematic illustrations. Some of the schematics were created using BioRender.com. The authors thank Parmeet Dhindsa from the Department of Electrical and Computer Engineering, Rice University, for helping with the laser heating experiment. The characterization equipment used in this project is from the Shared Equipment Authority (SEA) at Rice University.

Author contributions

M.M.R. conceived and coordinated the research. M.A.S.R.S. conducted, analyzed, and wrote the experimental results. M.A.S.R.S., Y.C., and V.H. designed 3D-printed bioreactors. M.A.S.R.S., S.B., and Y.C. synthesized the materials. S.H. assisted in writing the manuscript. I.R.S. and M.P. assisted in mechanical testing. M.B. and P.M.A. provided technical facilities. M.M.R. supervised the project, edited the manuscript, and was responsible for funding acquisition. All authors have read and approved the article.

Competing interests

The authors declare no competing interests.

Additional information

Supplementary information The online version contains supplementary material available at <https://doi.org/10.1038/s41467-025-60242-1>.

Correspondence and requests for materials should be addressed to Muhammad M. Rahman.

Peer review information *Nature Communications* thanks the anonymous reviewer(s) for their contribution to the peer review of this work. A peer review file is available.

Reprints and permissions information is available at <http://www.nature.com/reprints>

Publisher's note Springer Nature remains neutral with regard to jurisdictional claims in published maps and institutional affiliations.

Open Access This article is licensed under a Creative Commons Attribution-NonCommercial-NoDerivatives 4.0 International License, which permits any non-commercial use, sharing, distribution and reproduction in any medium or format, as long as you give appropriate credit to the original author(s) and the source, provide a link to the Creative Commons licence, and indicate if you modified the licensed material. You do not have permission under this licence to share adapted material derived from this article or parts of it. The images or other third party material in this article are included in the article's Creative Commons licence, unless indicated otherwise in a credit line to the material. If material is not included in the article's Creative Commons licence and your intended use is not permitted by statutory regulation or exceeds the permitted use, you will need to obtain permission directly from the copyright holder. To view a copy of this licence, visit <http://creativecommons.org/licenses/by-nc-nd/4.0/>.

© The Author(s) 2025